Electronic Supplementary Material (ESI) for Energy & Environmental Science.

Supporting Information

Establishing Reactivity Descriptors for Platinum Group Metal (PGM)-free Fe-N-C Catalysts for PEM Fuel Cells

Mathias Primbs[a‡], Yanyan Sun[a‡], Aaron Roy[b], Daniel Malko[c], Asad Mehmood[c], Moulay-Tahar Sougratib[2], Pierre-Yves Blanchard[b], Gaetano Granozzi[d], Tomasz Kosmalad,Giorgia Daniel[d], Plamen Atanassov[e], Jonathan Sharman[f], Christian Durante[d]*, Anthony Kucernak[c]*, Deborah Jones[b]*, Frédéric Jaouen[b]*, Peter Strasser[a]**

[a]Department of Chemistry, Chemical Engineering Division, Technical University of Berlin, 10623 Berlin, Germany

[b]ICGM, Univ. Montpellier, CNRS, ENSCM, Montpellier, France

[c]Department of Chemistry, Imperial College London, South Kensington SW7 2AZ London, United Kingdom

[d]Department of Chemical Sciences, University of Padova Via Marzolo 1, 35131 Padova, Italy

[e]Department of Chemical & Biomolecular Engineering and National Fuel Cell Research Center, University of California, Irvine, CA 92697, USA

[f]Johnson Matthey Technology Center, Blount's Court, Sonning Common, Reading RG4 9NH, United Kingdom

‡These authors contributed equally.

*E-mail: pstrasser@tu-berlin.de;
anthony@imperial.ac.uk;
Deborah.Jones@umontpellier.fr

frederic.jaouen@umontpellier.fr;

christian.durante@unipd.it;

jonathan.sharman@matthey.com

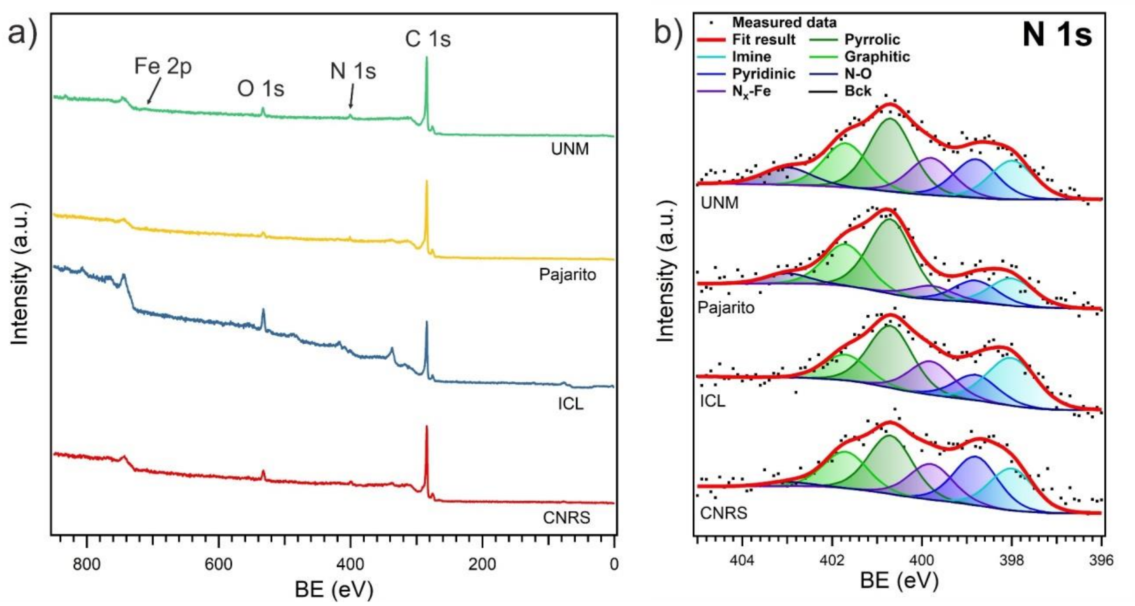

Figure S1. (a) XPS survey spectra and (b) high-resolution N 1s XPS spectrum for the benchmark catalysts.

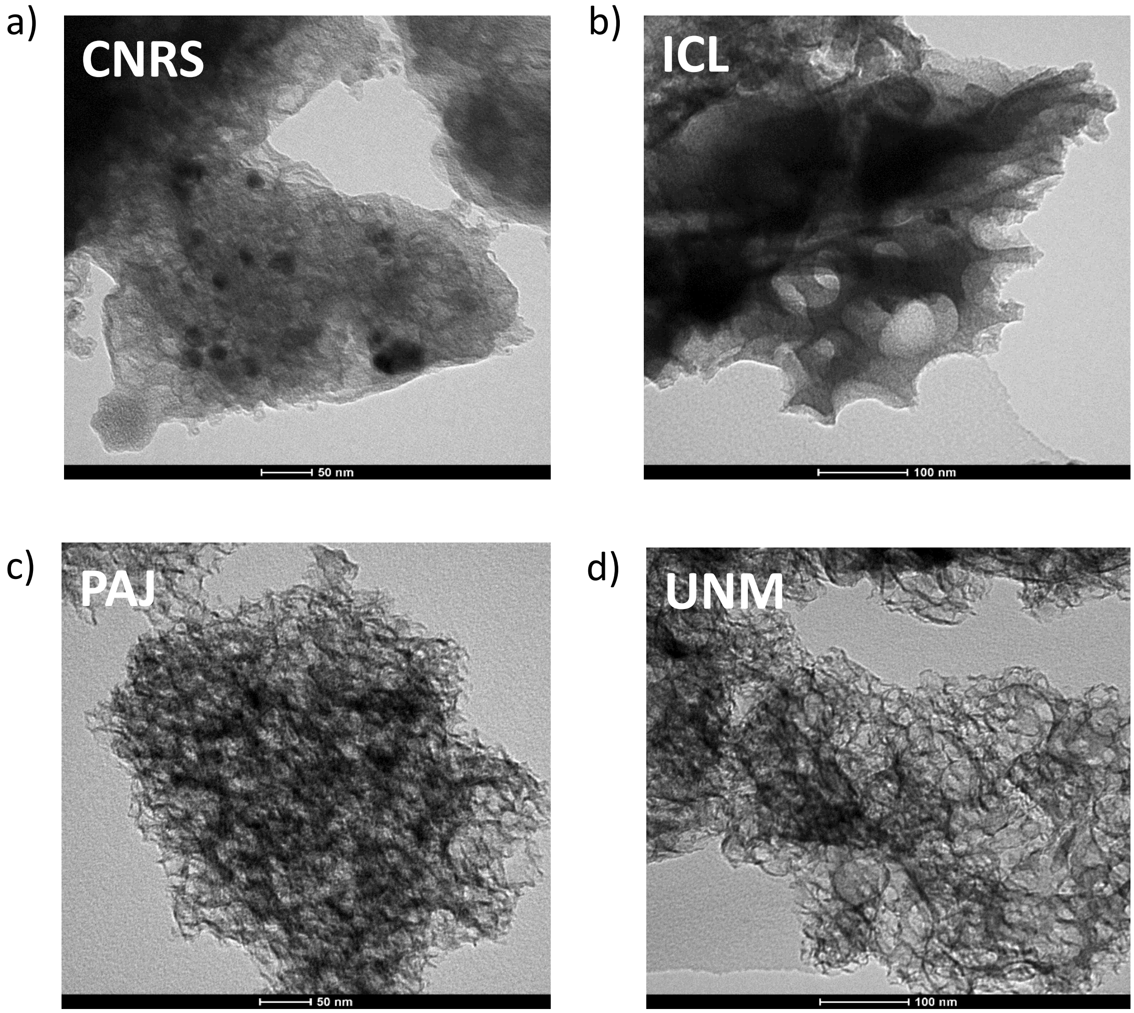

Figure S2. TEM images of the catalysts: (a) CNRS, (b) ICL, (c) PAJ and (d) UNM.

TEM measurements. TEM measurements were performed using a FEI Tecnai G2 transmission electron microscopy operating at 100 kV. The samples were dispersed in milli-Q water, sonicated for few minutes and dropped cast on a gold grid.

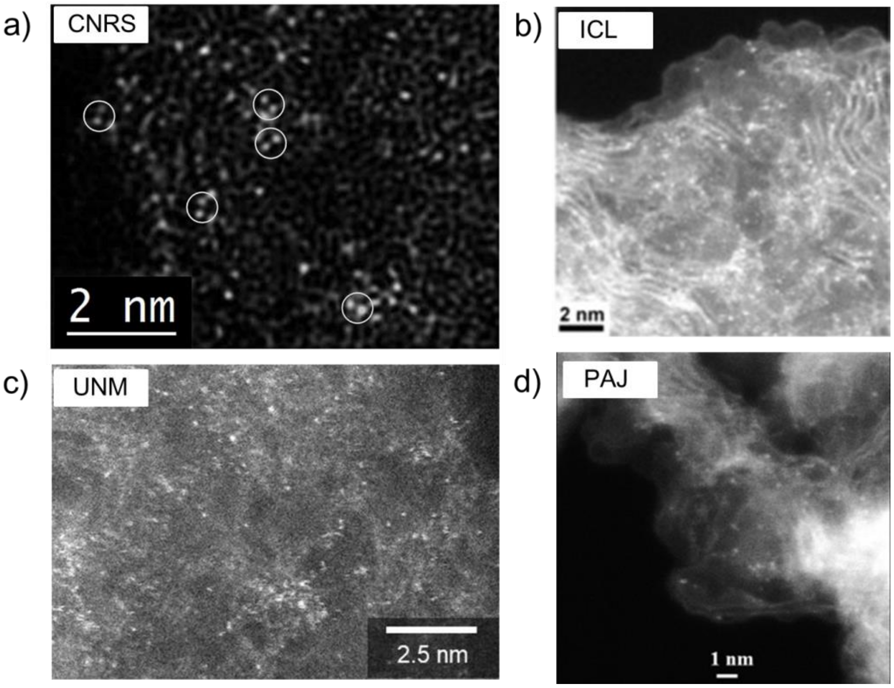

Figure S3. HAADF-STEM images of (a)) a catalyst prepared similarly to the CNRS catalyst of the present study but with less Fe content and containing only atomically dispersed Fe sites , (b) ICL, (c) UNM, and (d) PAJ catalysts. (a) Reprinted with permission ref. [1] Copyright 2018, The Royal Society of Chemistry; (b) reprinted with permission ref. [2] Copyright 2019 Elsevier Inc.; (c) reprinted with permission ref. [3] Copyright 2019, American Chemical Society; (d) reprinted with permission ref. [4] Copyright 2016, Wiley-VCH.

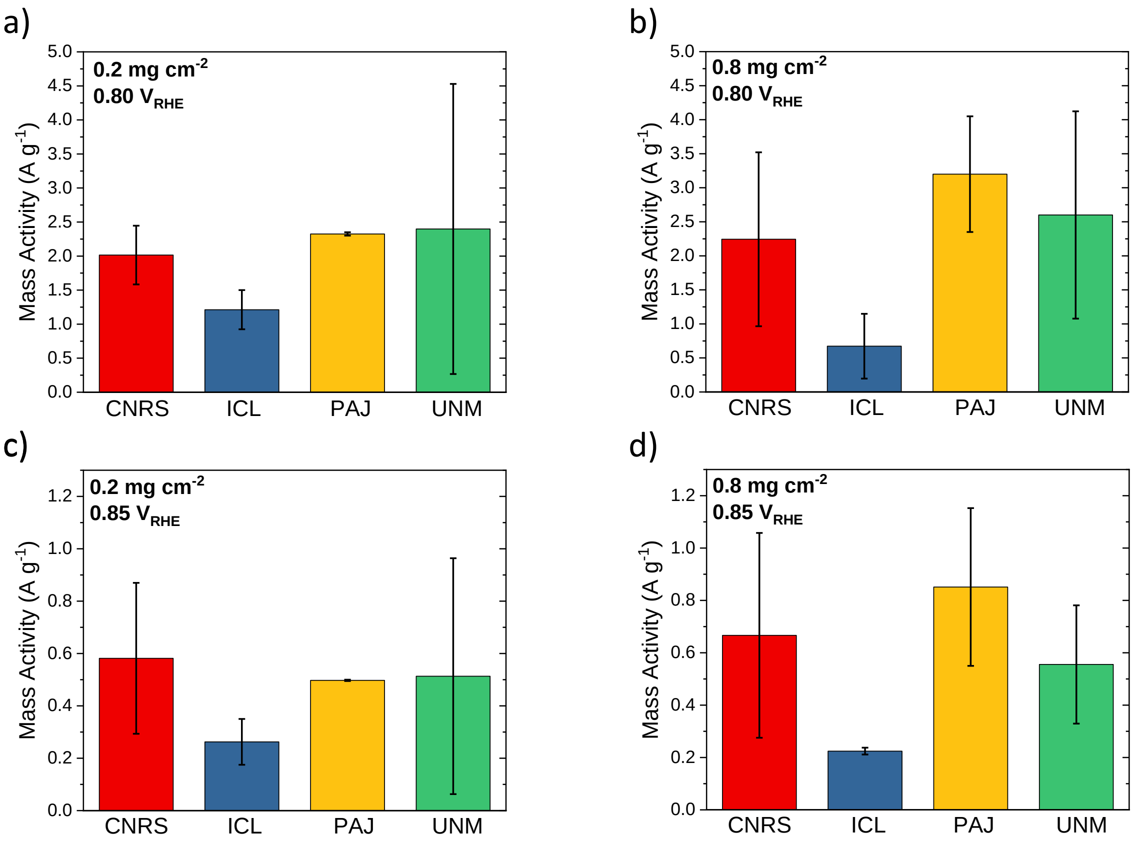

Figure S4. Initial ORR mass activity of the four catalysts as measured by RRDE for different catalyst loadings and applied potentials: (a) 0.2 mg cm^{-2} and 0.80 V$_{RHE}$, (b) 0.8 mg cm^{-2} and 0.80 V$_{RHE}$, (c) 0.2 mg cm^{-2} and 0.85 V$_{RHE}$, and (d) 0.8 mg cm^{-2} and 0.85 V$_{RHE}$. The electrolyte was 0.5 M H_2SO_4.

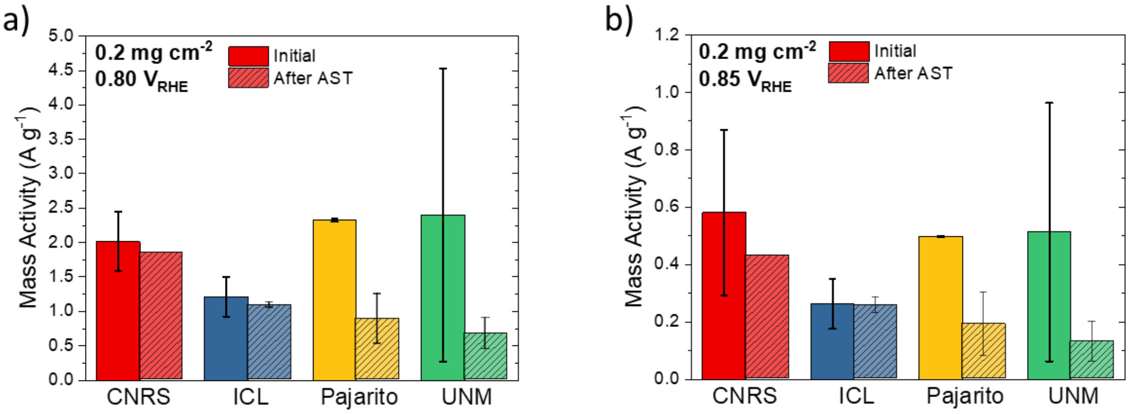

Figure S5. ORR mass activity before and after a load-cycling AST for a catalyst loading of 0.2 mg cm^{-2}: (a) mass activities at 0.80 V$_{RHE}$ and (b) mass activities at 0.85 V$_{RHE}$. The filled columns represent the initial activity and the hatched ones represent the activity after the AST (5,000 cycles between 0.6 and 0.9 V vs. RHE).

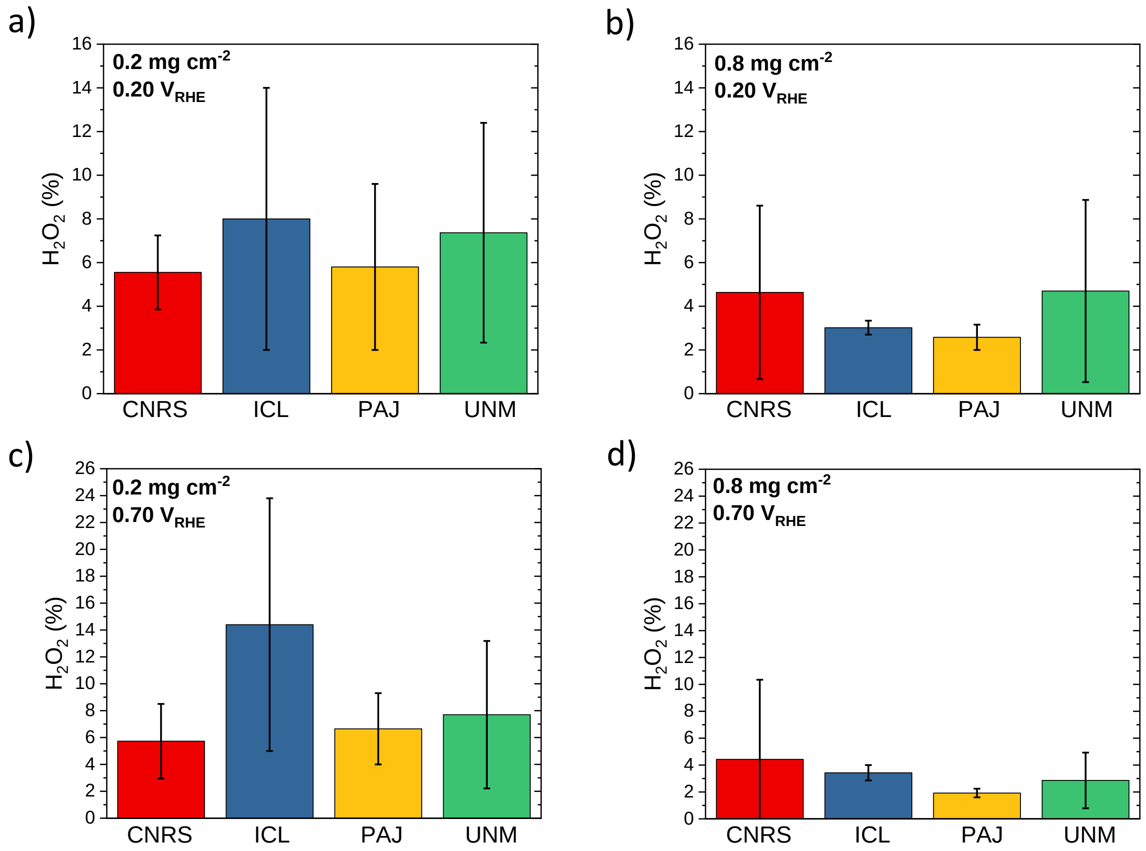

Figure S6. Hydrogen peroxide production (H_2O_2 %) during ORR of the four catalysts as measured by RRDE for two different catalyst loadings and two applied potentials: (a) 0.2 mg cm^{-2} and 0.20 V$_{RHE}$, (b) 0.8 mg cm^{-2} and 0.20 V$_{RHE}$, (c) 0.2 mg cm^{-2} and 0.70 V$_{RHE}$, and (d) 0.8 mg cm^{-2} and 0.70 V$_{RHE}$.

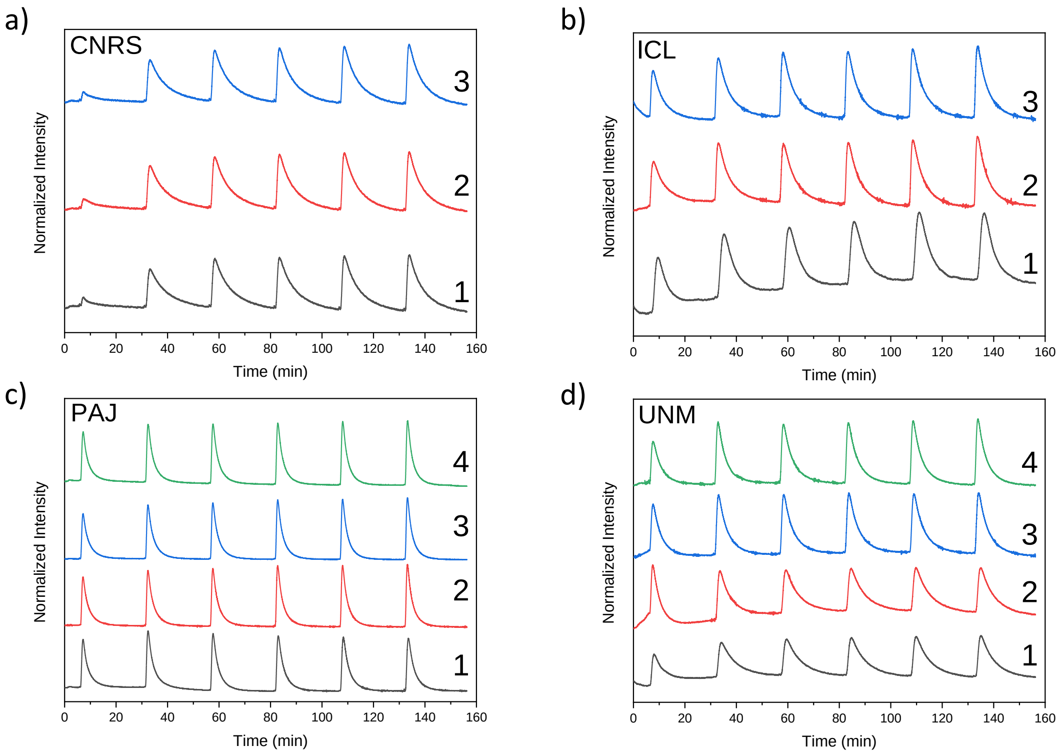

Figure S7. Repetitive CO pulse chemisorption profiles of the four benchmarking catalysts: (a) CNRS (3 repeats), (b) ICL (3 repeats), (c) PAJ (4 repeats), and (d) UNM (4 repeats). Surface CO saturation was achieved after *ca* 3 pulses. Reduced pulse peak area indicate CO uptake.

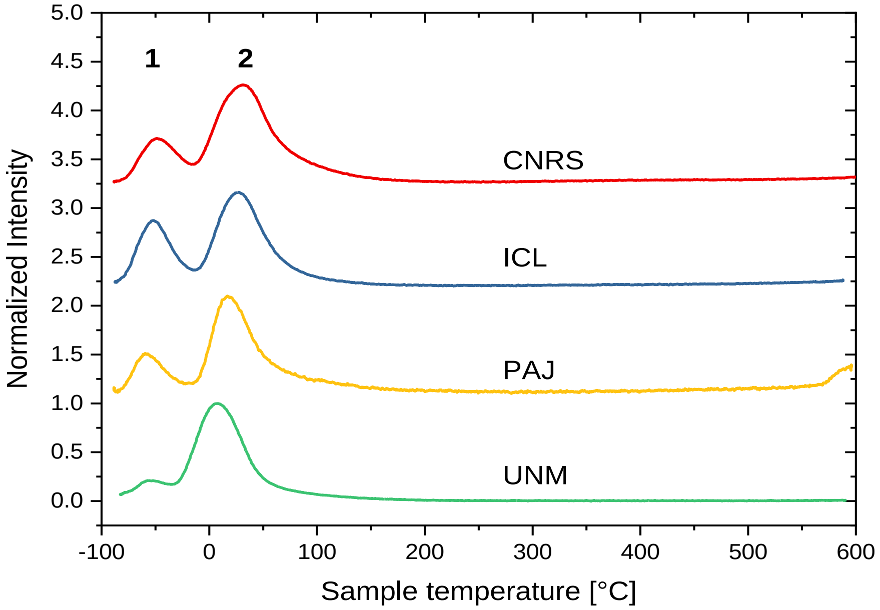

Figure S8. Temperature-programmed desorption (TPD) profiles in the range from -80 to 600 °C after saturation of the Fe surface sites with CO. TPD was conducted to get more insights about the chemical bonding between CO and catalytic active sites, where two obvious peaks are observed. It should be here highlighted that only the second desorption peak at high temperature corresponds to the binding of CO molecule on FeN_x centres in the Fe-N-C catalysts whereas the first peak at lower temperature should be attributed to the desorption of pre-adsorbed air resulting from the porous structure of the Fe-N-C catalysts. Interestingly, the CO desorption temperature of peak 2 follows the increasing order of UNM, PAJ, ICL, and CNRS, which may be explained by the different average Fe coordination geometry or different average oxidation state and/or spin state of the iron sites.

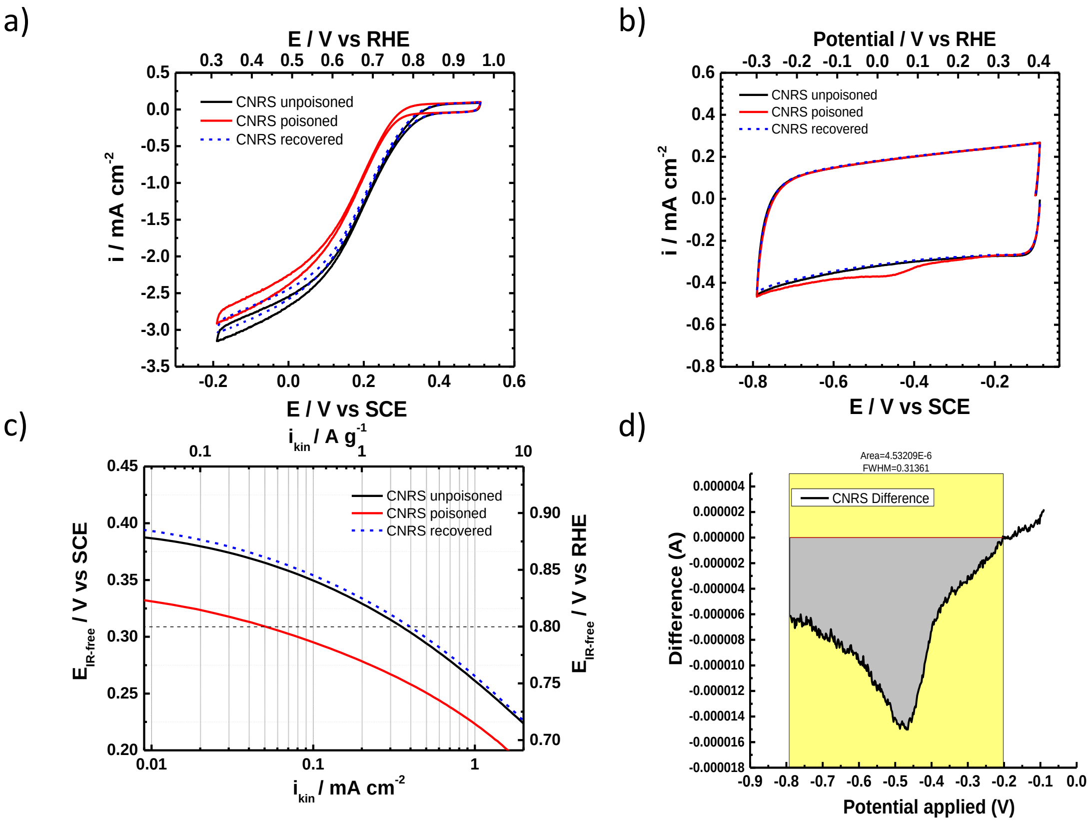

Figure S9. Rotating disk electrode measurement of CNRS catalyst before and after nitrite poisoning and its recovery. (a) ORR measurement in O_2-saturated electrolyte at the scan rate of 5 mV s^{-1}. (b) Stripping voltammetry in N_2-saturated electrolyte at 10 mV s^{-1}. (c) The kinetic current densities derived from the ORR measurement. (d) Excess current associated with the reductive stripping of nitrite. All measurements were performed in 0.5 M acetate buffer at pH 5.2 at 1600 rpm and the catalyst loading was 0.2 mg cm^{-2}.

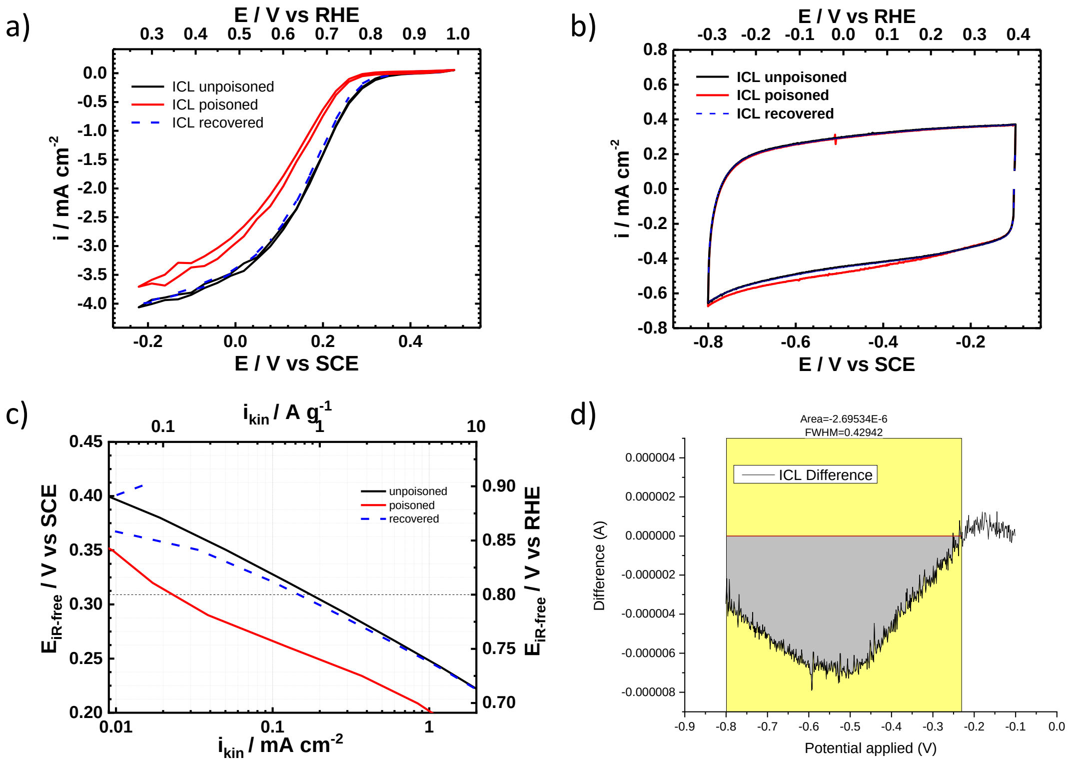

Figure S10. Rotating disk electrode measurement of ICL catalyst before and after poisoning and recovery. (a) ORR measurement in O_2-saturated electrolyte at the scan rate of 5 mV s^{-1}. (b) Stripping voltammetry in N_2-saturated electrolyte at 10 mV s^{-1}. (c) The kinetic current densities derived from the ORR measurement. (d) Excess current associated with the reductive stripping of nitrite. All measurements were performed in 0.5 M acetate buffer at pH 5.2 at 1600 rpm and the catalyst loading was 0.2 mg cm^{-2}.

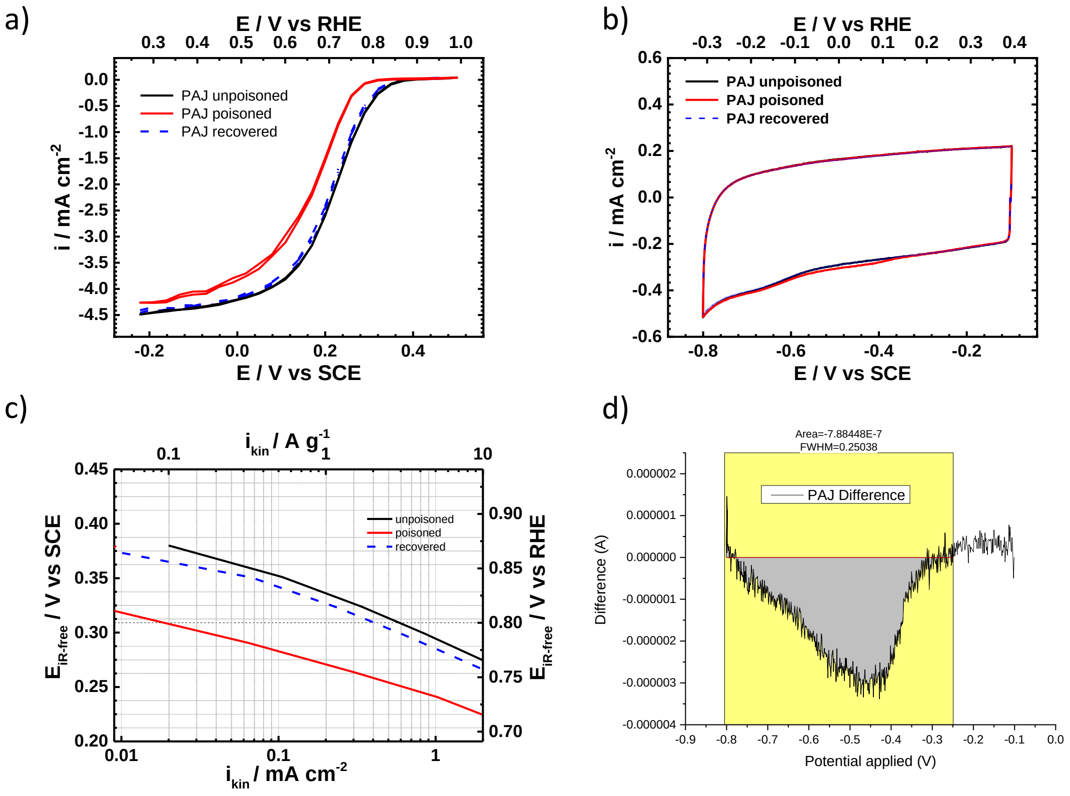

Figure S11. Rotating disk electrode measurement of PAJ catalyst before and after poisoning and recovery. (a) ORR measurement in O_2-saturated electrolyte at the scan rate of 5 mV s^{-1}. (b) Stripping voltammetry in N_2-saturated electrolyte at 10 mV s^{-1}. (c) The kinetic current densities derived from the ORR measurement. (d) Excess current associated with the reductive stripping of nitrite. All measurements were performed in 0.5 M acetate buffer at pH 5.2 at 1600 rpm and the catalyst loading was 0.2 mg cm^{-2}.

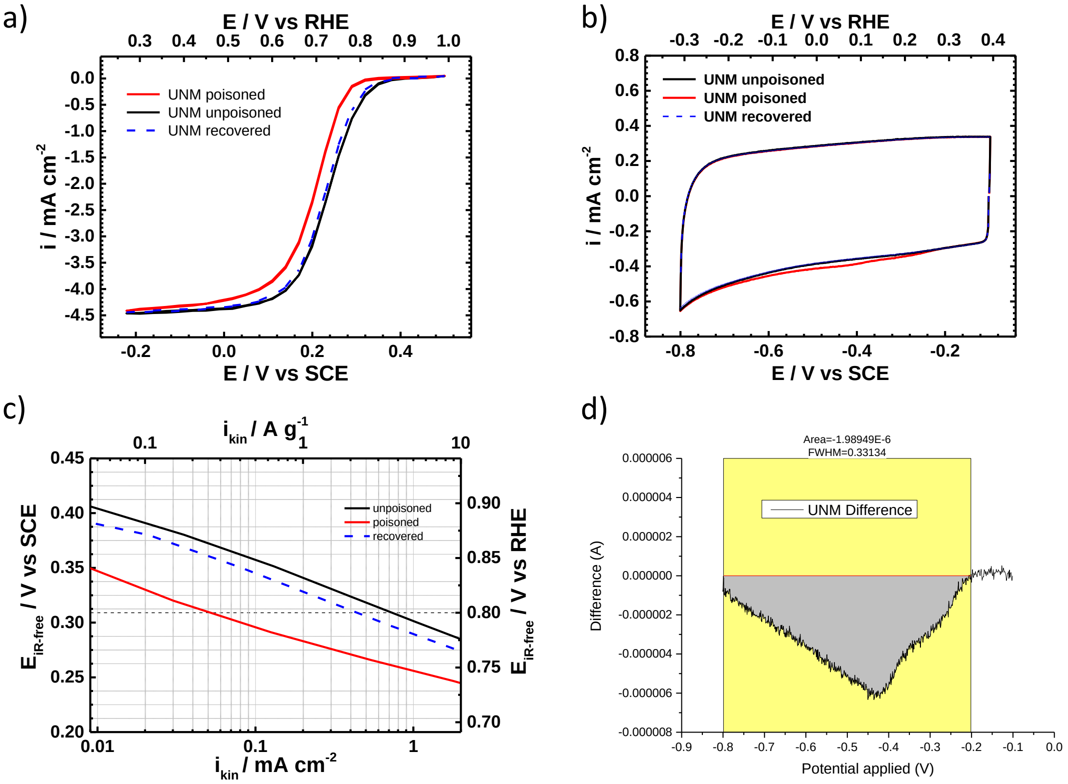

Figure S12. Rotating disk electrode measurement of UNM catalyst before and after poisoning and recovery. (a) ORR measurement in O_2-saturated electrolyte at the scan rate of 5 mV s^{-1}. (b) Stripping voltammetry in N_2-saturated electrolyte at 10 mV s^{-1}. (c) The kinetic current densities derived from the ORR measurement. (d) Excess current associated with the reductive stripping of nitrite. All measurements were performed in 0.5 M acetate buffer at pH 5.2 at 1600 rpm and the catalyst loading was 0.2 mg cm^{-2}.

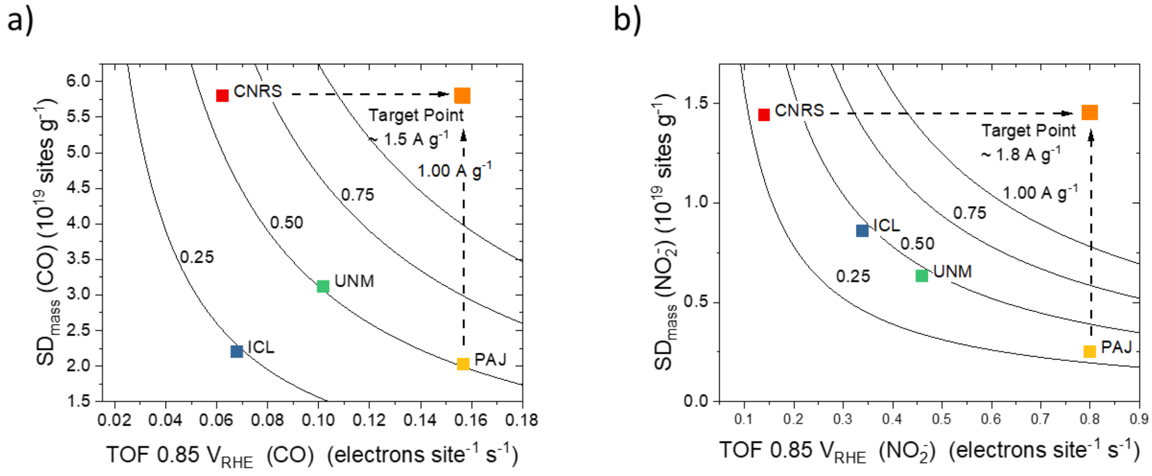

Figure S13. Mass SD-TOF reactivity maps at 0.85 V_{RHE}: The mass-based Fe surface site density (SD_{mass}) plotted against the TOF for each catalyst. Points of constant activity (iso activity curves) shown in grey with units of A g^{-1} at 0.85 V_{RHE}: (a) SD_{mass}(CO) – TOF reactivity map, derived from CO chemisorption and (b) SD_{mass}(NO_2^-) – TOF reactivity map derived from nitrite stripping values.

The correlation between the catalytic active site density and TOF at the potential of 0.85 V_{RHE} was also plotted (**Figure S14**). Different rankings in the mass activity are observed, that is, ICL< UNM ≈ PAJ < CNRS with the CO chemisorption method whereas CNRS ≈ PAJ < ICL ≈ UNM in the nitrite stripping method, which may be due to different calculation methods for kinetic current in the CO chemisorption and nitrite stripping method. Nevertheless, with both methods, the CNRS and PAJ catalysts were located the extreme place in terms of catalytic active site density and TOF. Further, the correlation of surface area corrected catalytic active site density with TOF was also investigated, and the different trend in regards of areal catalytic activity is also observed in the CO chemisorption and nitrite stripping method (**Figure S15**). Meanwhile, the ICL catalyst exhibited more active sites (more kinetic current per surface area) compared to the CNRS catalyst despite the fact that both catalysts possessed almost the same areal catalytic site density.

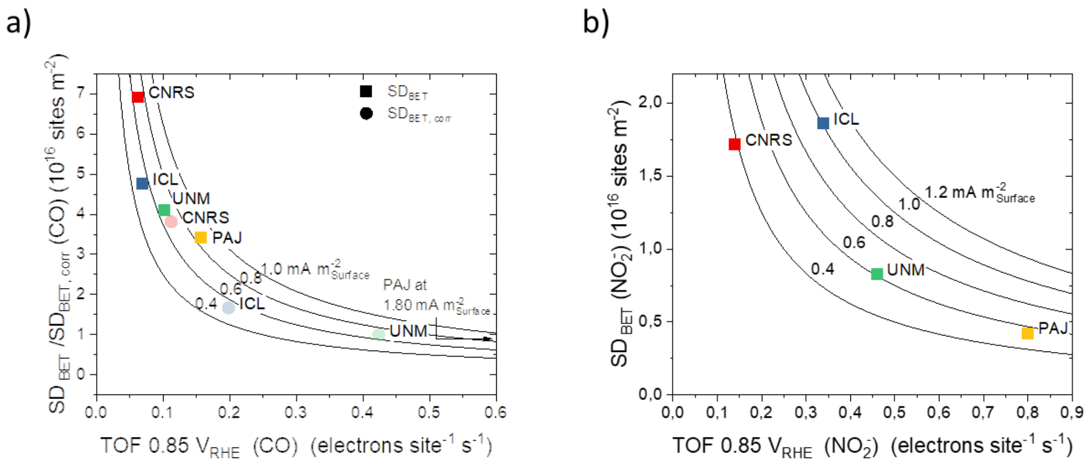

Figure S14. Areal SD-TOF reactivity maps at 0.85 V_{RHE}: The areal Fe surface site density (SD) plotted against the TOF for each catalyst. Points of constant activity (iso activity curves) shown in grey with units of mA m^{-2} at 0.85 V_{RHE}: (a) SD_{BET} (CO) – TOF reactivity map, derived from CO chemisorption and (b) SD_{BET} (NO_2^-) – TOF reactivity map derived from nitrite stripping.

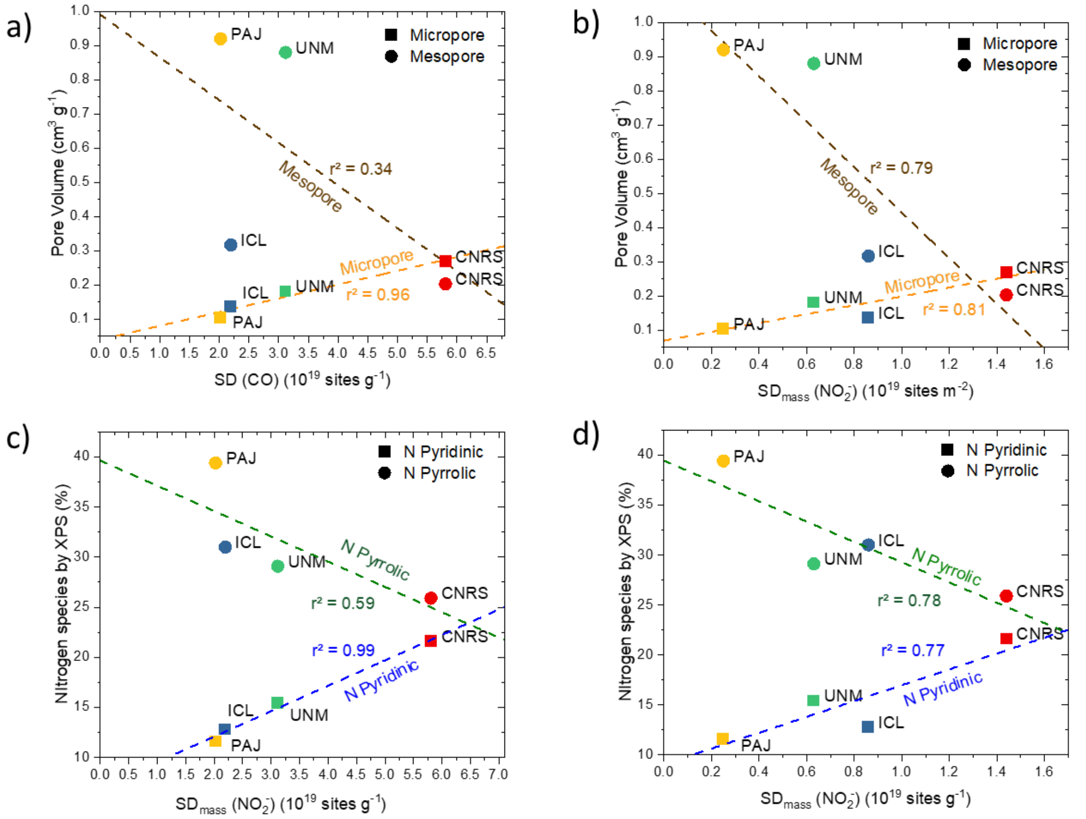

Figure S15 Correlation of catalytic active site density via (a, c) CO chemisorption and (b, d) nitrite stripping method with (a, b) pore volume and (c, d) nitrogen species from XPS results.

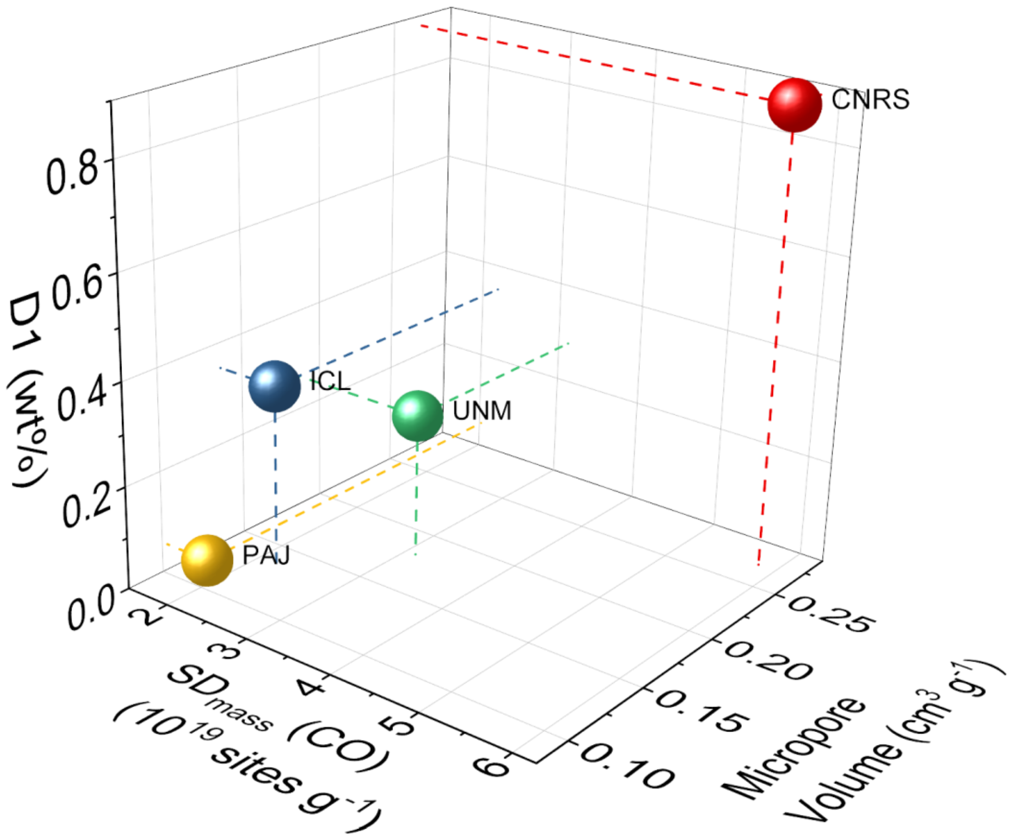

Figure S16 Correlation of the bulk weight ratio of the molecular Fe D1 moiety, derived from ^{57}Fe Mößbauer spectra, with the micropore volume, and the Fe surface site density, SD_{mass} (CO) derived from CO-chemisorption method.

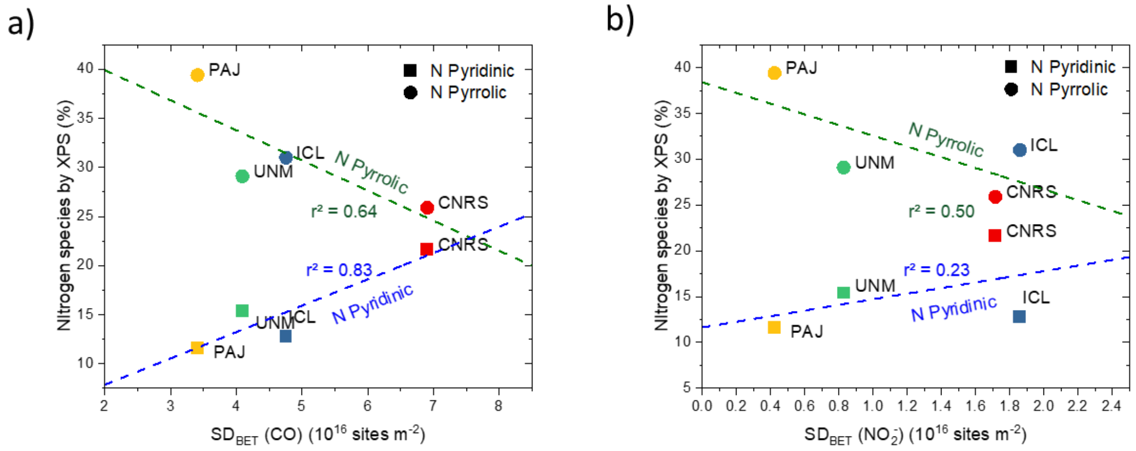

Figure S17 Correlation of the areal catalytic active site density via (a) CO chemisorption and (b) nitrite stripping method with nitrogen species including pyridinic-N and pyrrolic-N.

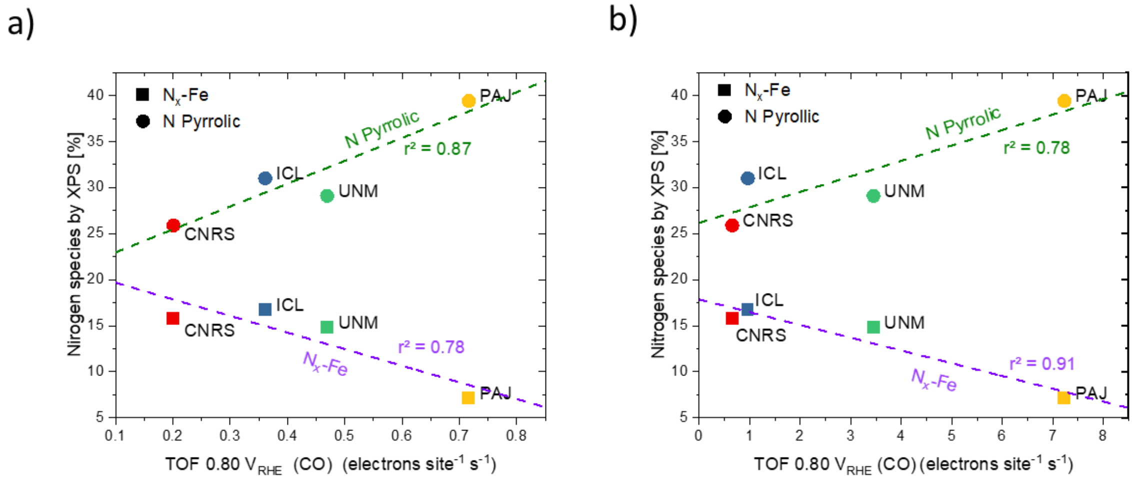

Figure S18. Correlation of experimental TOF values with the ratio of Fe-N_x and Pyrrolic nitrogen species. TOF values were derived from (a) CO cryo-adsorption and (b) nitrite stripping. N species ratios were determined from N1s XPS. Data measured at at 0.80 $V_{RHE.}$

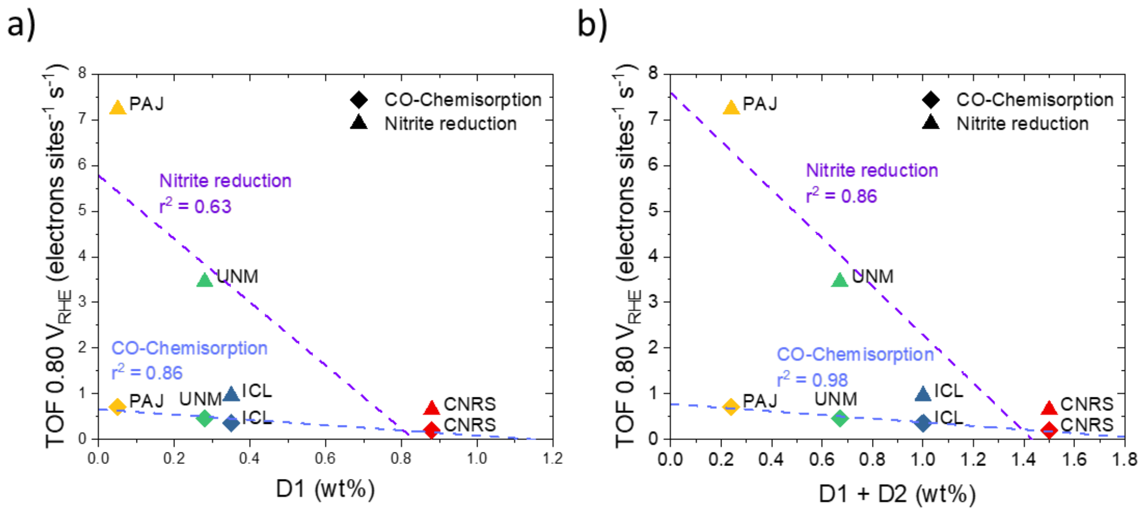

Figure S19. Correlations between TOF values at 0.80 V_{RHE} derived from CO chemisorption and nitrite stripping and the Mössbauer-derived weight of Fe sites a) D1, b) sum of D1 and D2

Quantitative correlation between SD (CO) and SD (NO_2^-).

The x-intercept of the regression line in Figure 4b, here reproduced as **Figure S20a,** is about 3.1×10^{16} sites m^{-2} and may be interpreted as the amount of BET-normalized Fe surface site density, SD_{BET}(CO), that remained inaccessible to *in-situ* reductive NO_2^- / NO stripping. The inaccessibility is in part based on the lower probe molecule chemisorption energy (see CO-TPD analysis of the four catalysts in **Figure S8**), which makes sampling of these sites under *in-situ* ambient conditions in the presence of liquid electrolyte impossible. Subtracting the NO-inaccessible portion of SD_{BET}(CO) from the experimental SD_{BET}(CO) values then yields corrected $SD_{BET.\ corr}$ (CO) values (**Figure S20b**), which display a perfect quantitative 1:1 correlation with the corresponding $SD_{BET}(NO_2^-)$ values for catalysts with a balanced ratio of meso- and micropore volumes. The quantitative deconvolution and correlation of independent, experimental *in-situ* and *ex-situ* SD values represents an important step forward in the accurate evaluation of catalytically active surface single-Fe sites.

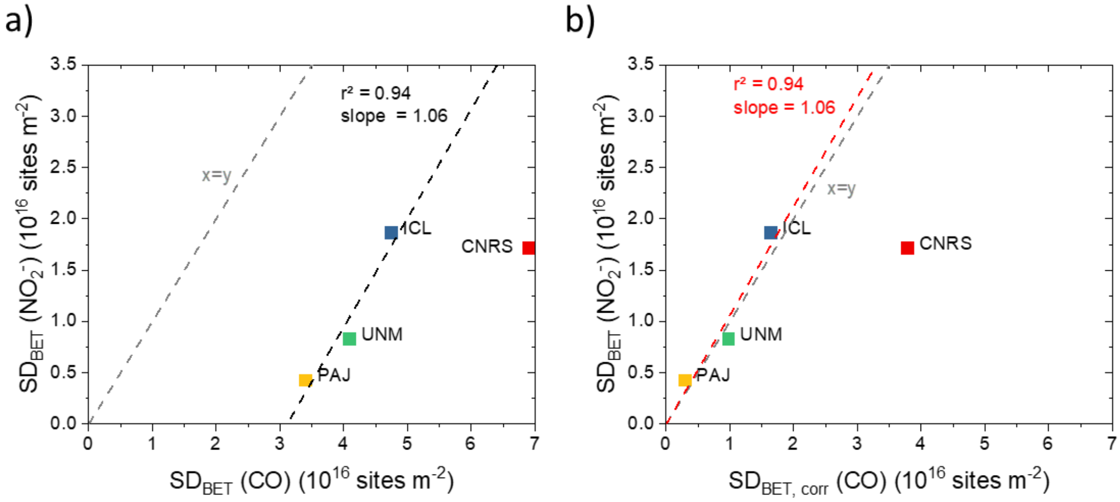

Figure S20. Correlations of ex-situ and in-situ Fe surface site density (SD) values of four PGM-free Fe-N-C ORR catalysts obtained using CO-chemisorption and nitrite electrochemical reductive stripping (a) SD_{BET} values measured in situ vs. SD_{BET} values measured ex situ with a regression line in points PAJ, UNM and ICL (b) SD_{BET} (NO_2^-) values versus x-intercept-subtracted $SD_{BET,corr}$ (CO) values. The x=y line are given as grey dashed lines.

Table S1. Mössbauer analysis results of the four selected benchmarking catalysts: CNRS, ICL, PAJ, and UNM.

Material	Assignment	IS mm/s	QS mm/s	LW mm/s	H Tesla	Area %	Lamb-Mössbauer factor	Relative amount of each component to all Fe(1) %	Wt % Fe of each component(2) % wt
CNRS	γ-Fe	-0.08	-	0.34	-	10	0.78	14	0.36
	Fe_3C	0.185	-	0.35	20	3	0.67	4	0.09
	α-Fe	0	-	0.36	33	18	0.67	22	0.55
	D1	0.34	1.03	0.72	-	42	0.46	35	0.88
	D2	0.45	2.48	1.50	-	27	0.52	25	0.62
ICL	D1	0.36	0.96	0.73	-	38	0.46	35	0.35
	D2	0.55	2.2	1.75	-	62	0.52	65	0.65
PAJ	γ-Fe	-0.12	-	0.35	-	36	0.78	45	0.27
	α-Fe	0	-	0.21	33.2	15	0.67	16	0.1
	D1	0.37	0.75	0.9	-	11	0.46	8	0.05
	D2	0.40	2.34	1.81	-	38	0.52	31	0.19
UNM	γ-Fe	-0.08	-	0.37	-	11	0.78	16.36	0.13
	D1	0.36	1.1	0.72	-	40	0.46	35.07	0.28
	D2	0.41	2.77	1.53	-	49	0.52	48.57	0.39

Note: IS is the isomer shift (reported vs. an α-Fe foil reference at room temperature), QS the quadrupole splitting, LW the line width and H the hyperfine field, describing the singlet, doublet and sextet components used for the fittings. Area is the relative % of area corresponding to each fitted spectral component relative to the total absorption area. The column "relative amount of each component to all Fe" is derived from the knowledge of the area % of each spectral component of a given Fe-N-C catalyst (column "Area") and of the Lamb Mössbauer factors of each Fe species. It therefore includes the necessary correction of the γ-ray absorption area in order to account for the different probability of the recoilless absorption event for Fe atoms in different coordination environments. For each catalyst, the last column is derived from the multiplication of the next-to-last column by the total wt % Fe bulk content (measured by ICP).

Table S2. CO chemisorption and NO_2^- stripping data and derived quantities such as mass- and BET-normalized Fe surface site densities (SD_{mass} and SD_{BET}) and the turnover frequencies (TOF) at applied electrode potentials of +0.80 and +0.85 V_{RHE} for the four benchmarking catalysts.

Catalyst	**CNRS**		**ICL**		**PAJ**		**UNM**	
Method	**NO_2^-**	**CO**	**NO_2^-**	**CO**	**NO_2^-**	**CO**	**NO_2^-**	**CO**
CO uptake [nmol g^{-1}]	-	96 ± 1	-	36 ± 10	-	33.6 ± 0.6	-	52 ± 4
SD_{mass} [10^{19} sites g^{-1}]	1.44	5.80 ± 0.08	0.86	2.20 ± 0.6	0.25	2.02 ± 0.03	0.63	3.12 ± 0.2
BET surface area [m^2 g^{-1}]	840		463		593		763	
SD_{BET} [10^{16} sites m^{-2}]	1.71	6.90	1.86	4.76	0.42	3.41	0.83	4.10
TOF at 0.80 V_{RHE} [electrons $site^{-1}$ s^{-1}]	0.65	0.20	0.96	0.36	7.23	0.71	3.45	0.47
TOF at 0.85 V_{RHE} [electrons $site^{-1}$ s^{-1}]	0.14	0.06	0.34	0.08	0.80	0.16	0.46	0.10

Table S3. CO chemisorption derived site density values for the four benchmarking catalysts. $SD_{BET,corr}$ (CO) = (SD_{BET} (CO) − $SD_{BET,Intercept}$ (CO)) is the x-intercept of the BET-normalized Fe Surface site density in **Figure S20b** and represents the inaccessible portion of the Fe sites at ambient conditions; $SD_{BET,corr}$ is the corrected Fe surface site density derived from CO chemisorption after subtraction of the inaccessible portion of the Fe sites at ambient conditions.

Method	**CNRS**	**ICL**	**PAJ**	**UNM**
SD_{mass} [10^{19} sites g^{-1}]	5.80 ± 0.08	2.20 ± 0.6	2.02 ± 0.03	3.12 ± 0.2
SD_{BET} [10^{16} sites m^{-2}]	6.90	4.76	3.41	4.10
$SD_{BET,Intercept}$ (CO) [10^{16} sites m^{-2}]	3.11	3.11	3.11	3.11
$SD_{BET,corr}$ (CO) [10^{16} sites m^{-2}]	3.79	1.65	0.30	0.98

References

1. C. H. Choi, H.-K. Lim, M. W. Chung, G. Chon, N. Ranjbar Sahraie, A. Altin, M.-T. Sougrati, L. Stievano, H. S. Oh, E. S. Park, F. Luo, P. Strasser, G. Dražić, K. J. J. Mayrhofer, H. Kim and F. Jaouen, *Energy & Environmental Science*, 2018, **11**, 3176-3182.
2. D. Malko, Y. Guo, P. Jones, G. Britovsek and A. Kucernak, *Journal of Catalysis*, 2019, **370**, 357-363.
3. T. Asset, S. T. Garcia, S. Herrera, N. Andersen, Y. Chen, E. J. Peterson, I. Matanovic, K. Artyushkova, J. Lee, S. D. Minteer, S. Dai, X. Pan, K. Chavan, S. Calabrese Barton and P. Atanassov, *ACS Catalysis*, 2019, **9**, 7668-7678.
4. J. Xie, K. Yin, A. Serov, K. Artyushkova, H. N. Pham, X. Sang, R. R. Unocic, P. Atanassov, A. K. Datye and R. J. Davis, *ChemSusChem*, 2017, **10**, 359-362.